Towards Numerical Simulation of Cavitating Flows in Complex Geometries

M. Mattson and K. Mahesh
(Aerospace Engineering and Mechanics, University of Minnesota)

Introduction

This paper discusses our efforts at simulating large systems of bubbles in complex geometries, with specific application to modeling cavitation instabilities. An important unstable regime is the transition from sheet-to-cloud cavitation (SCC). Experiments performed by Callenaere *et al.* (2001) highlight the unsteady flow structures of SCC, which is characterized by unstable regions of vapor bubbles that suddenly appear near the leading edge of a hydrofoil. These bubble "clouds" violently collapse as the free-stream pressure increases downstream of inception. This collapse leads to unsteady loading and emanates intense acoustic waves. Also, experiments by Ceccio (personal communication) will investigate drag reduction in marine applications by injecting an air jet from the face of a backward-facing step. The air jet is more stable and therefore considered more effective at drag reduction than a layer of micro-bubbles. This paper investigates two methods to simulate and predict such flows: **I.** a one-way coupled Lagrangian bubble model and **II.** the force coupling method (Lomholt *et al.*, 2002) which is extended to account for bubble volume variation. In both methods, the bubble dynamics are governed by the Rayleigh-Plesset (RP) equation, which is integrated in time using a fourth-order accurate Runge-Kutta solver (RK4) with adaptive time stepping. The bubble models are coupled with a robust, unstructured, DNS carrier phase solver. This paper describes our numerical approaches and compares results between one-way and two-way coupling in channel flows.

One-way coupled Euler-Lagrangian approach

In the one-way coupled Euler-Lagrangian framework, the bubbly flow is modeled as a dispersed phase, with individual bubbles treated as point particles governed by an equation for bubble motion, combined with a continuous carrier phase described by DNS / LES Navier-Stokes equations. To solve the Navier-Stokes equations for the continuous phase, a finite-volume approach for unstructured grids (Mahesh *et al.*, 2004) is used. This algorithm assumes constant density of the carrier phase and solves the incompressible Navier-Stokes equations using a predictor-corrector approach. This algorithm is discretely energy conserving to ensure robustness at high Reynolds numbers. This method is able to simulate large numbers of bubbles in complex flows. Each bubble is tracked individually and is characterized by its instantaneous position, velocity and size. Assuming the bubble size is much smaller than the length scales of motion in the carrier phase, the bubbles are approximated as spherical nuclei.

Various forces from the carrier fluid act upon the bubble. These are applied to the bubble's center of mass. The bubble Reynolds number is assumed to be small. Also, due to the bubble's small size and dilute concentration, it does not exert an appreciable force on the carrier fluid or other bubbles. This is the one-way coupling regime. Under these assumptions, Maxey & Riley (1983) derived an equation for small, rigid spheres. However, as a bubble encounters pressure variations in the flow it will respond by changing it volume. The Rayleigh-Plesset equation is used to determine the instantaneous bubble radius as a function of pressure in the carrier fluid. A fourth-order Runge-Kutta solver with adaptive time-stepping is used to ensure accurate and efficient integration of the Rayleigh-Plesset equation. To account for volume variation effects on the bubble trajectory, an additional term by Johnson & Hsieh (1966) is added to the Maxey & Riley formulation to obtain

$$
\begin{aligned}
\frac{dV_i}{dt} = & -2g_i + 3 \left.\frac{Du_i}{Dt}\right|_{\vec{Y}(t)} + \frac{u_i - V_i}{\tau_b} \\
& + \left[\left(\vec{u} - \vec{V}\right) \times \vec{\omega}\right]_i + \frac{3}{R}\left(u_i - V_i\right)\frac{dR}{dt},
\end{aligned}
\tag{1}
$$

with the Stokes relaxation time defined as

$$
\tau_b = \frac{m_f}{12\pi R\mu} = \frac{R^2}{9\nu}.
\tag{2}
$$

To advance the bubble position in time, a 2nd-order Adams-Bashforth time integrator is used. The bub-
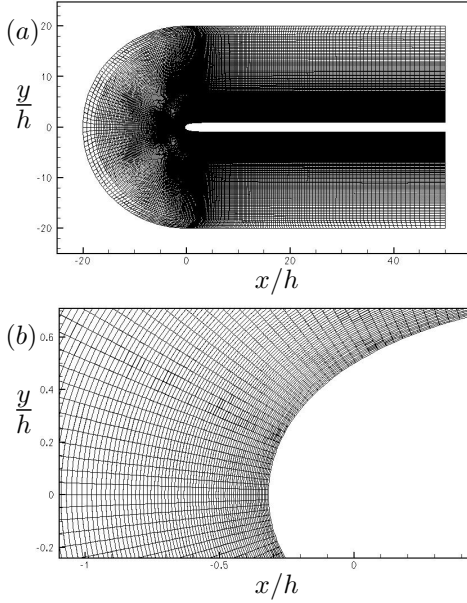
Figure 1: Unstructured mesh generated for simulation of gas nuclei flowing over a blunt body.

ble is advanced in time for every update of the bubble radius. The material derivative of the fluid velocity is obtained (Eqn. 3) at the bubble center with a tri-linear interpolation in space and linear interpolation in time. The fluid velocity, pressure and vorticity are also interpolated to the instantaneous bubble location using the tri-linear method.

$$\frac{Du_i}{Dt}\bigg|_{\vec{Y}(t)} = \left(\frac{\partial u_i}{\partial t} + u_j \frac{\partial u_i}{\partial x_j}\right)\bigg|_{\vec{x}=\vec{Y}(t)} \qquad (3)$$

This approach can simulate flows with large numbers of bubbles in complex geometries and over a wide range of Reynolds numbers. By using the Rayleigh-Plesset equation to describe the radial response of the bubble, this model can be extended to flows with large pressure fluctuations (such as cavitating flows). Including the Rayleigh-Plesset ordinary differential equation provides some numerical challenges, especially when solving systems with large numbers of bubbles since it must be solved for each individual bubble. The bubble oscillation timescales can become much smaller than the timescales of the carrier fluid. To solve the RP equation, a variable-timestep 4th order accurate (in time) Runge-Kutta integration scheme is applied. This allows resolution of the small bubble timescales during oscillations with small, accurate timesteps and also boosts efficiency by increasing the timestep when the bubble is near equilibrium (Babu, 2007).

Gas nuclei trajectories over a blunt body

Johnson & Hsieh (1966) numerically studied gas nuclei traversing a two-dimensional blunt body. Assuming potential flow for the fluid, Johnson & Hsieh obtained an analytical solution for fluid velocity and pressure. A Lagrangian equation for bubble dynamics was derived and coupled with the fluid phase to obtain an ordinary differential equation for the bubble motion.

Using the Euler-Lagrangian model coupled with the single-phase Navier-Stokes solver, similar results are obtained while not assuming potential flow. The bubbles are assumed to be small and spherical, with a radius that can vary due to pressure fluctuations. Bubbles are injected upstream of the blunt body. They then travel downstream and around the obstacle in response to the pressure gradient and drag forces. In an Euler-Lagrangian framework, the bubble velocity is given in Johnson & Hsieh (1966) as

$$\frac{dV_i}{dt} = -3\frac{\partial p}{\partial x_i} + \frac{3}{R}\left(u_i - V_i\right)\frac{dR}{dt}$$
$$+ \frac{18Re_b}{R^2 Re_f}\frac{C_D}{24}\left(u_i - V_i\right). \qquad (4)$$

The first term on the right hand side in Eqn. 4 is the pressure gradient term. The bubbles are repulsed from areas of increasing pressure and attracted by favorable pressure gradients. The second term includes volume variation effects. For this problem, the volume variation term is neglected, as in Johnson & Hsieh (1966). The last term includes the bubble drag. An empirical relation for the drag coefficient of small, spherical particles by Haberman & Morton (1953) is used.

$$C_D = \frac{24}{R}\left(1 + 0.197Re_b{}^{0.63} + 2.6\times10^{-4}Re_b{}^{1.38}\right) \qquad (5)$$

Note that as $Re_b \to 0$ then the drag relation approaches the Stokes limit of $C_D = 24/R$. The bubble Reynolds number (Re_b), fluid Reynolds number (Re_f), Weber number (We) and the vapor cavitation number (σ_v) are defined as

$$Re_b = \frac{R\left|u_i - V_i\right|}{\nu}, \quad Re_f = \frac{hU_o}{\nu},$$

$$We = \frac{\rho_f U_o{}^2 R_o}{S}, \quad \sigma_v = \frac{p_o - p_v}{\rho_f U_o{}^2/2},$$

with h defined as the width of the blunt body, and U_o as the freestream velocity value. Simulating the Reynolds number given by Johnson & Hsieh ($Re_f =$
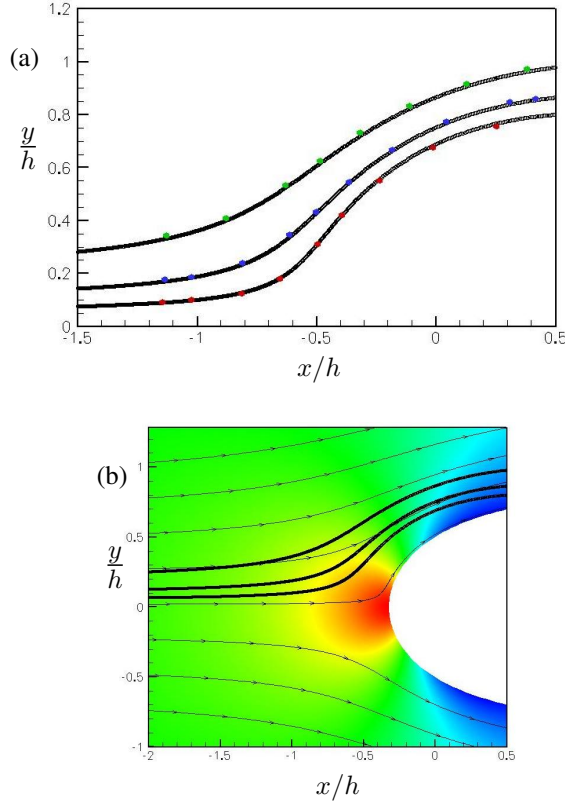
Figure 2: Comparison of bubble trajectories to Johnson & Hsieh, with $\sigma_v = 0.4$. The data by Johnson & Hsieh is given in (a) by the filled circles, with $y_o/h = 0.05$ (•), $y_o/h = 0.1$ (•) & $y_o/h = 0.2$ (•). Figure (b) plots bubble trajectories along with pressure color contours and velocity streamlines. Red represents high pressure and blue low pressure.

$238,095$) requires resolving the very thin laminar boundary layer. To reduce the computational requirements, the fluid Reynolds number was reduced to a level that is reasonable to resolve but still achieves good agreement with the analytic velocity field.

After progressively increasing the Reynolds number, results showed that a Reynolds number of $Re^* = 10^4$ provides good agreement for the flow field. The bubble velocity equation and Re_b still retain the original viscosity term. Also, the vapor cavitation number (σ_v) is 0.4 and the Weber number is 976. The vapor pressure p_v is assumed to be negligible, so the reference pressure term becomes $p_o = \sigma_v \rho_f U_o^2 / 2$.

The grid contains $261,600$ hexagonal control volumes, with an initial wall-normal distance of $0.005h$. The grid extends from $-25 \leq x/h \leq 50$ and $-25 \leq y/h \leq 25$. Three control volumes resolve the space between the periodic faces (in the z-direction). Figure 1 depicts the resolution of the mesh. Figure 1a shows the grid in its entirety, while Figure 1b shows the boundary layer resolution.

Three bubbles are introduced at a streamwise distance of $x_o/h = -10$, and injected at three different vertical positions ($y_o/h = 0.2, 0.1$ & 0.05). The bubbles follow the streamlines until they approach the blunt body. The bubbles are then repelled from the blunt body by the adverse pressure gradient and no longer follow the fluid streamlines. Also, the bubble radii are decreasing in the high pressure regions as the bubble attempts to achieve pressure equilibrium. Eventually the bubble trajectory brings it around the bluff body into the low-pressure region, where the bubble grows. Figure 2a plots the bubble trajectories and demonstrates good agreement between the Euler-Lagrangian simulation (black dots) and the Johnson & Hsieh results (large colored dots). The colors represent the initial injection position, with red dots for $y_o/h = 0.05$, blue dots for $y_o/h = 0.1$ and green dots for $y_o/h = 0.2$. Fluid streamlines, pressure color contours and bubble trajectories are given in Figure 2b. The color contour gives the relative pressure magnitude, over a scale from high (red) to low (blue). In comparing to the numerical investigation by Johnson & Hsieh, the Euler-Lagrangian method coupled with the Rayleigh-Plesset equation accurately reproduces results for the flow of gas nuclei about a blunt body.

Force coupling method

An alternative to the Euler-Lagrangian approach is the approximate force coupling method (FCM). This method has been developed and tested recently by Maxey *et al.* (1997), Maxey & Dent (1998), Dent (1999), Lomholt (2000), Maxey & Patel (2001) and Lomholt *et al.* (2002). It extends the Euler-Lagrangian formulation from one--way coupling to two-way coupling without needing to resolve the smallest scales of the flow near the bubbles. As in the one-way coupled Euler-Lagrangian framework, the bubbly flow is modeled as a dispersed phase, with individual bubbles treated as point particles governed by an equation for bubble motion, combined with a continuous carrier phase described by DNS / LES Navier-Stokes equations. To solve the Navier-Stokes equations for the continuous phase, the finite-volume approach by Mahesh *et al.* (2004) is used. Each bubble is tracked individually and is characterized by its instantaneous position, velocity and size.

Considering N number of spherical particles, the coupling is implemented as a source term in the momentum equation. The force and/or torque exerted by each bubble on the carrier phase can be described by a force monopole (F_i) and a force dipole (F_{ij}) and act as an equal and opposite force and/or torque on the bubble itself. The entire domain, including the volume occupied by the par-
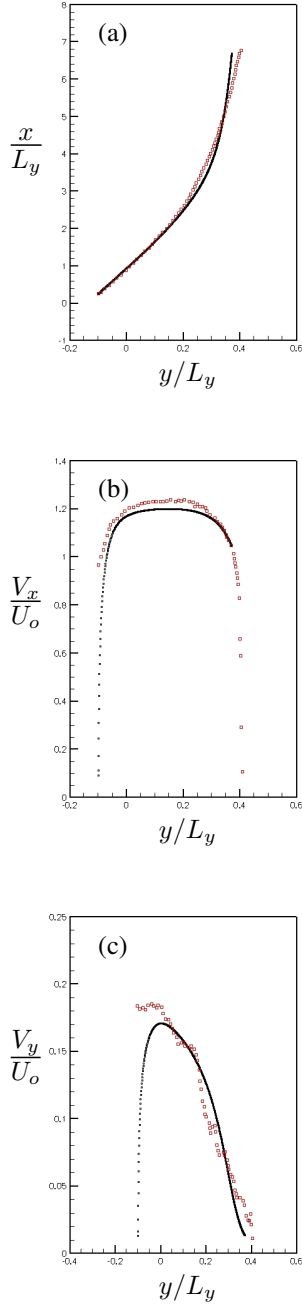
ticles, is considered an incompressible fluid and governed by

$$\frac{\partial u_i}{\partial x_i} = 0, \tag{6}$$

$$\rho_f \left(\frac{\partial u_i}{\partial t} + u_j \frac{\partial u_i}{\partial x_j} \right) = \frac{\partial p}{\partial x_i} + \mu \frac{\partial^2 u_i}{\partial x_j \partial x_j}$$
$$+ \sum_{n=1}^{N} \left[F_i^n \Delta_m(\vec{x} - \vec{Y}^n) + F_{ij}^n \frac{\partial \Delta_d(\vec{x} - \vec{Y}^n)}{\partial x_i} \right]. \tag{7}$$

The fluid velocity is given as u, fluid density as ρ_f, fluid pressure as p and μ denotes the fluid dynamic viscosity. As a first approximation, fluid torque and strain acting from the fluid on the bubble are ignored and the force dipole term is neglected. The force monopole term is integrated over the entire domain and normalized by the Gaussian envelope function

$$\Delta_m(\vec{x} - \vec{Y}^n) = \frac{1}{(2\pi\sigma^2)^{3/2}} \times$$
$$\exp\left(-\frac{(x_i - Y_i^n)(x_i - Y_i^n)}{2\sigma^2} \right), \tag{8}$$

which decreases exponentially as the distance from the bubble centroid increases. The Gaussian term (σ) is related to the bubble radius by

$$\sigma = \frac{\sqrt{\pi}}{R} \approx \frac{1.77}{R}. \tag{9}$$

The force monopole is equal and opposite to the body force from the fluid applied to the bubble. In general, this force is

$$F_i^n = V_p (\rho_p - \rho_f) \left(g_i - \frac{\mathrm{d}V_i^n}{\mathrm{d}t} \right), \tag{10}$$

where V_p denotes the bubble volume, ρ_b the bubble density, ρ_f the fluid-phase density and $\vec{g}$ the gravitational acceleration. An extra forcing term, not included in this iteration, may be included to restrict bubbles from occupying the same volume. For this paper it is assume that buoyancy dominates the inertial forces, and only the gravity term is used. The bubble velocity $\vec{V}^n$ is obtained through localized averaging of the fluid velocity and given by

$$V_i^n(t) = \tilde{u}_i = \int u_i(\vec{x}, t) \Delta \left(\vec{x} - \vec{Y}^n \right) d^3\vec{x}. \tag{11}$$

Figure 3: Comparison of bubble trajectories and velocities with experiment. The simulation quantities are represented by small black square (□) and experimental quantities are represented by larger red squares (□). Figure (a) plots the advance of the particle position, while figures (b) and (c) plot the particle streamwise and stream-normal velocities vs. y-position, respectively.

Table 1: Experimental values

Case	$\rho_f(\mathrm{g/cm^3})$	$\rho_p(\mathrm{g/cm^3})$	$\theta(^\circ)$	$\nu(\mathrm{mm^2/s})$
1	1.115	1.081	8.23	3.125

Table 2: Domain parameters

Case	$L_x \times L_y \times L_z$	$N_x \times N_y \times N_z$
1	$10 \times 1 \times 4$	$512 \times 48 \times 96$

For both the bubble velocities and force monopole, the Gaussian envelope function is integrated over the entire domain. To advance the bubble position in time, a 2nd-order Adams-Bashforth time integrator is used. The bubble position is integrated every fluid timestep. The force coupling method thus efficiently models the two-way coupling between the bubble and the fluid.

Single sphere rising in an inclined channel

The force coupling method is validated for a single solid sphere rising in an inclined channel. A corresponding experiment was performed by Lomholt *et al.* (2002), with a setup composed of a rectangular channel with height $L_x = 150$ mm, width $L_y = 10$ mm and depth $L_z = 100$ mm. A single particle is released near the center of the channel and tracked using a standard CCD camera. From the visual data, particle position and velocity can be determined. The channel can be rotated about the spanwise axis by an angle θ to achieve the desired configuration. A mixture of glycerol and water was used for the fluid to achieve the desired fluid properties. The particles were polymid spheres with a uniform, known density and size. The particle has a constant radius $R/L_y = 0.1$. Tables 1, 2 and 3 show the physical and computational parameters used.

The computational grid is uniform and has N_x, N_y and N_z control volumes in each respective spatial dimension. The grid is periodic in the spanwise and streamwise directions. Increasing mesh resolution or reducing timestep was observed to have no effect on the simulation results. The Reynolds number scaling based on the Stokes setting velocity W is defined as

$$Re_p^S = \frac{2RW}{\nu} = \frac{2R}{\nu} \left| \frac{2R^2}{9\mu} \left(\rho_p - \rho_f \right) g \right|$$
$$= \frac{4R^3}{9\nu^2} \left| \frac{\rho_p}{\rho_f} - 1 \right| g.$$

(12)
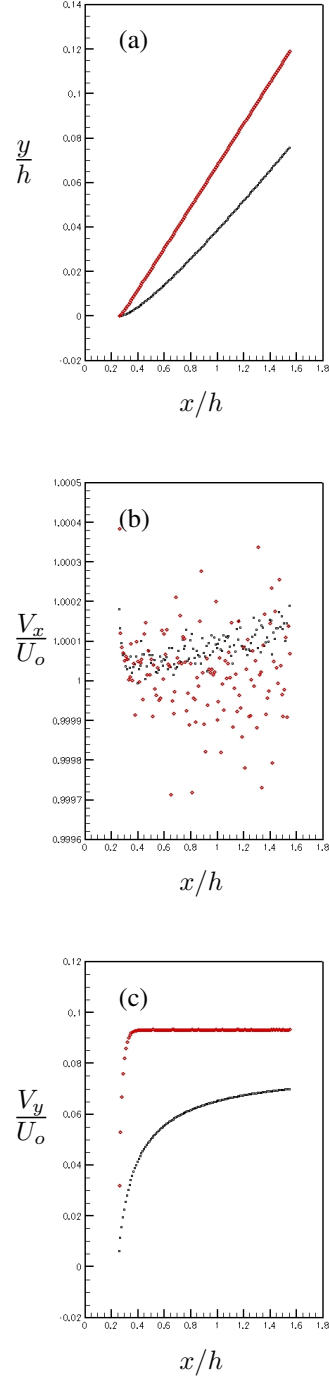

Figure 4: Comparison of two modeling approaches for $Re_f = 85.45$. The force coupling method quantities are represented by black squares ($\square$) and the Euler-Lagrangian results are represented by red diamonds ($\lozenge$). Figure (a) plots the advance of the bubble position, while figures (b) and (c) plot the bubble streamwise and stream-normal velocities vs. y-position, respectively.

Table 3: Non-dimensional parameters

Case	$Re_f = L_y U_o / \nu$	$Fr = |g| L_y / U_o{}^2$	Re_p^S
1	32.0	982.0	13.6

Table 5: Physical parameters (ctd.)

Case	U_o(m/s)	$p_o \times 10^{-5}$(Pa)	R(mm)
1	0.1	1	0.05
2	0.1	1	0.05

Figure 3 compares the computational results to experiment. Computational results are depicted with small black squares and experimental results are larger red squares. Figure 3a plots the streamwise particle position versus wall-normal position, while Figures 3b and 3c plot the streamwise and wall-normal particle velocities, respectively.

The experimental and computational results show fair agreement. Due to buoyancy, the particle initially ($y/L_y < 0.2$) moves in the direction of the gravitational acceleration. For $y/L_y < 0.2$, the computed particle follows the experimental trajectory, although the streamwise velocity is somewhat lower. As the particle approaches the wall, the rise velocity decreases. Here the computed wall-normal velocity is first higher, then lower, than the experimental values. This results in the slight trajectory differences. As the particle continues to approach the wall ($y/L_y > 0.2$) both the streamwise and wall-normal velocities decrease. Eventually the particle comes to rest as it contacts the wall. Including dipole forces in the force coupling method formulation would better resolve the fluid stresses as the particle nears the wall and lead to more accurate results (Lomholt *et al.*, 2002). As a first approximation, the monopole force coupling method is reasonably accurate and efficient.

Comparing the FCM and EL approaches

The two approaches are compared for laminar flow. The first computation simulates a single bubble rising in a uniform flow, and the second models the injection of a bubble/air mixture in laminar channel flow. For these simulations, parameters were chosen to reflect laminar flow of small bubbles in seawater. The dimensional values are shown in Tables 4 and 5 and domain and non-dimensional parameters are given in Tables 6 and 7. The single bubble problem is listed in the tables as Case 1 and the laminar injection problem as Case 2. In the injection problem, the

Table 6: Domain parameters

Case	$L_x \times L_y \times L_z$	$N_x \times N_y \times N_z$
1	$4 \times 1 \times 0.5$	$192 \times 48 \times 24$
2	$2 \times 2 \times 1$	$98 \times 98 \times 48$

difficulties involve resolving high concentrations of bubbles and requires modeling bubble-fluid interactions. The one-way coupled EL approach does not account for this two-way coupling effect, while the FCM approach models the interaction to a reasonable accuracy. Due to the effects of large bubble concentrations, we see differences between the EL and FCM approaches.

Single bubble rising in a uniform flow

A single bubble rising in a channel with uniform streamwise velocity is simulated using both approaches. A slip velocity of unity is implemented at the walls to ensure uniform velocity near the boundaries. The bubble is introduced near the inflow at $x/h = 0.25$ and $y = z = 0$. The simulation is run with a constant timestep on a uniform grid. The bubble radius is initialized as $R/h = 0.05$ and remains constant for the duration of the simulation. Refining the grid or reducing the timestep does not change the results. The bubble travels downstream and rises due to buoyancy. As the bubble approaches a constant terminal velocity, the bubble Reynolds number, Re_b, becomes small and we approach the Stokes flow regime. In the Stokes regime, the bubble reaches a terminal velocity of $(gd_b{}^2)/(18\nu) \approx 0.92$. Figure 4 plots results for $Re_f = 85.45$. Differences between the different models can be seen in the position and V_y velocity plots, while both exhibit equal streamwise velocities. The EL simulation reaches terminal velocity much earlier than the FCM simulation and also approaches the theoretical Stokes ter-

Table 4: Physical parameters

Case	ρ_f(g/cm^3)	S(N/m)	ν(mm^2/s)	h(mm)
1	1.03	0.00734	1.17	2
2	1.03	0.00734	1.17	2

Table 7: Non-dimensional parameters

Case	We	Re_f	Fr	Re_p^S
1	0.07	85.45	1.964	0.8
2	0.07	85.45	1.964	0.8

Figure 5: Fluid velocity color contours at a planar cut of $z/h = 0$ in laminar channel flow. Bubble positions are represented by circles.
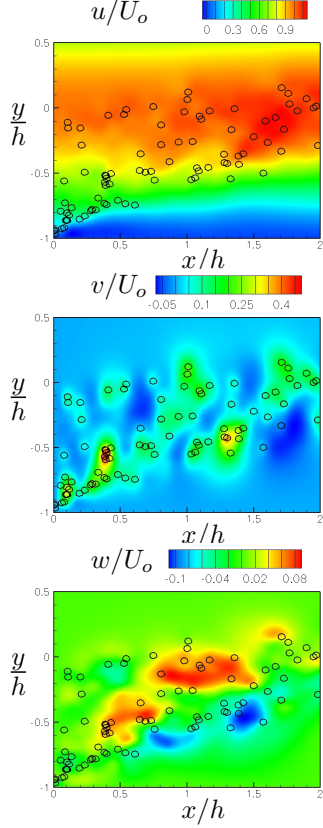

Figure 6: Fluid vorticity color contours at a planar cut of $z/h = 0$ in laminar channel flow. Bubble positions are represented by circles.

minal velocity. In the FCM approach, the streamwise velocity is resolved but the V_y component is less than the Stokes limit. This is primarily due to the same feature that can be seen in the FCM validation results. For a low Re_p^S, viscous stresses and strains become important and the force dipole should be included in the general fluid equation for FCM. Since the dipole and higher-order force coupling terms are neglected, the stresses around the bubble is not entirely resolved, resulting in a reduced terminal velocity for the monopole results. This simulation was also performed with $Re_f = 10$ and $Re_f = 1$ and no significant improvement of differences between the EL and FCM approaches were observed.

Bubble injection into laminar channel flow

This section compares the EL and FCM models for laminar channel flow with high bubble concentration. Bubbles (at equilibrium) are introduced randomly into the bottom half of the inflow of a laminar channel. The top and bottom boundaries are zero-slip walls and the spanwise boundaries are p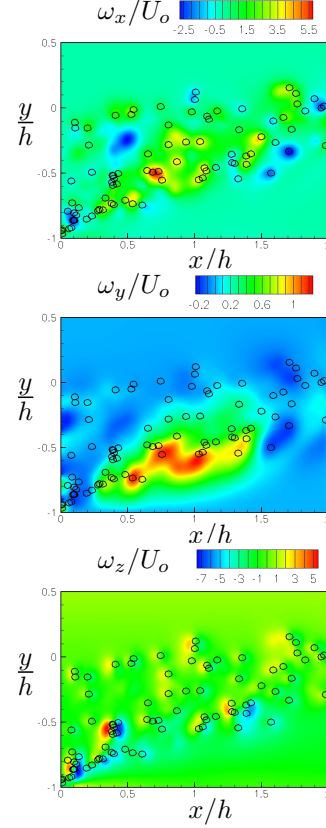eriodic. A zero-gradient boundary condition is applied for the outflow plane. The point-particle Euler-Lagrangian and force coupling method are run in tandem to compare results. Due to two-way coupling effects, differences exist between the results of each method.

The laminar channel is initialized with a parabolic streamwise velocity profile. A parabolic V_x profile is continuously specified at the inflow plane. A constant timestep of $\Delta t = 0.0002$ is used, and a bubble is injected randomly into the bottom half of the inflow plane every 15 timesteps. This simulation was run for 15000 timesteps. Figures 5-8 show the results from the force coupling method results at timestep 15000. Each figure represents a planar cut of the domain and the relevant fluid parameter plotted using a color contour, along with the position of bubbles within a distance of one radii from the respective cut.

The bubbles rise as they are carried from left to right by the streamwise momentum. For the bubbles, the pressure changes are small and each bubble radius remains nearly constant. Bubbles with low streamwise velocity (near the bottom wall) accumulate near the wall
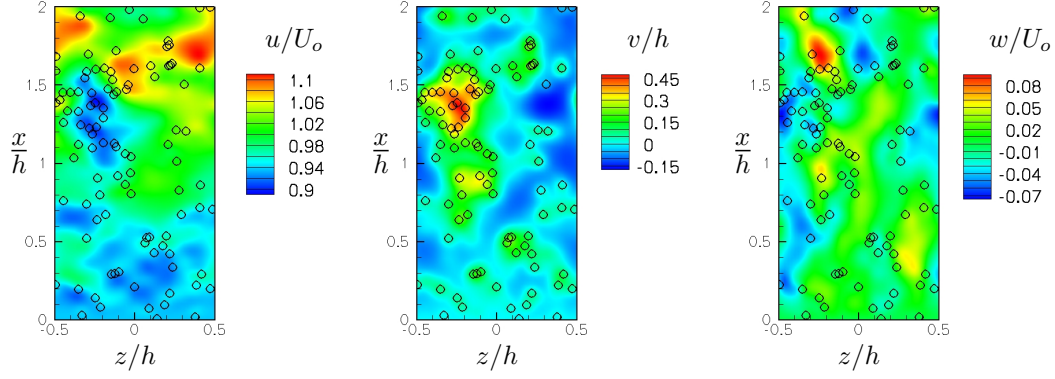
Figure 7: Fluid velocity color contours at a planar cut of $y/h = -0.25$ in a laminar channel. Bubble positions are represented by circles.
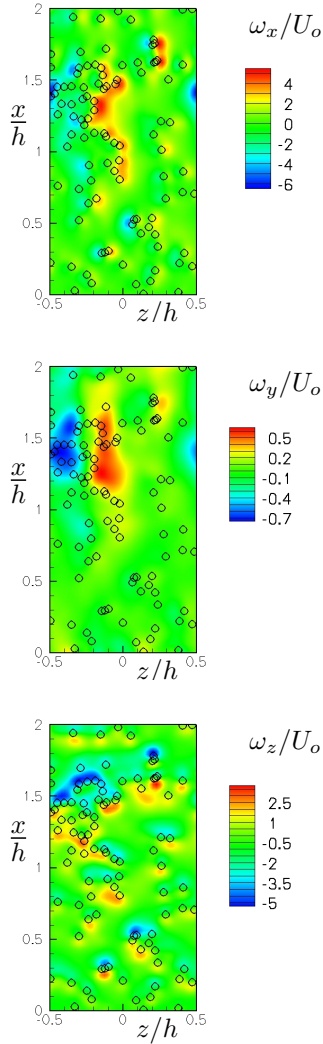

Figure 8: Fluid vorticity color contours at a planar cut of $y/h = -0.25$ in a laminar channel. Bubble positions are represented by circles.

but eventually rise and become entrained into the higher-speed flow. The fluid streamlines deviate from their initial orientation (pointing directly downstream) due to the rising bubbles influencing the fluid flow. Figure 5 plots the fluid velocities and Figure 6 plots the fluid vorticity in the plane $z/h = 0$. The flow is clearly three-dimensional, though the streamwise momentum still dominates the flow. A small grouping of bubbles propel themselves upwards quite dramatically at $(x/h, y/h) = (0.4, -0.55)$. The close proximity of the bubbles creates an additive effect of each bubble in the force coupling to produce the strong rise velocity.

In Figure 6 the x and z components of vorticity are dominant, with ω_z appearing "dipole-like" around bubble clusters. For example, each bubble cluster has a local maximum of ω_z on its left-hand side, and a local minimum on its right-hand side. These are due to the strong gradients in the V_y velocity, both in the streamwise and spanwise directions. Figures 7-8 show results for an $x-z$ planar cut at $y/h = -0.25$. The flow is clearly three-dimensional. Portions of the flow-field with grouping of bubbles tend to have larger rise velocities than individual bubbles themselves. The dominant x and z components of vorticity are also observed here and due to the strong gradients of V_y. In comparison, the one-way coupled EL approach does not predict the three-dimensionality of the flow since there is no mechanism for the bubble to act on the fluid phase.

A comparison of results shows differences between the EL and FCM methods for the bubble behavior. In general, both show the bubbles rising as they are carried downstream. However, near the bottom wall at the injection plane, higher concentrations of EL bubbles reside and persist for some distance downstream. The force coupling method modifies the flow and causes the low-momentum layer near the wall to grow towards midstream. This implies that the FCM bubbles near the wall are more inclined
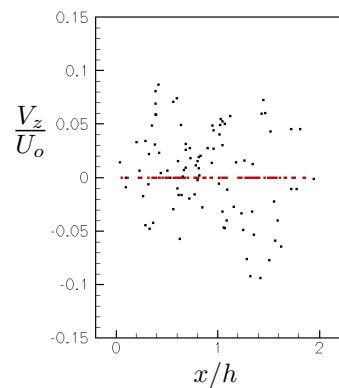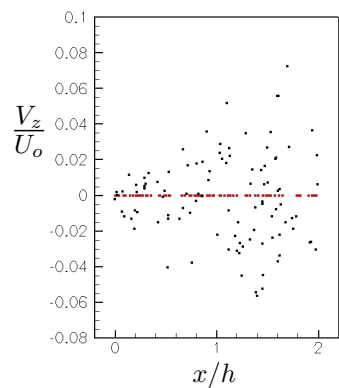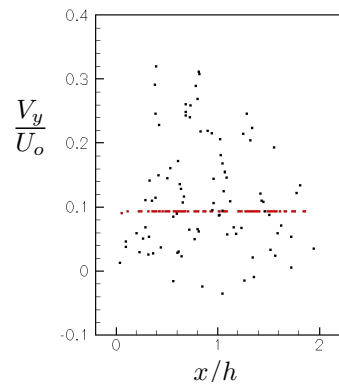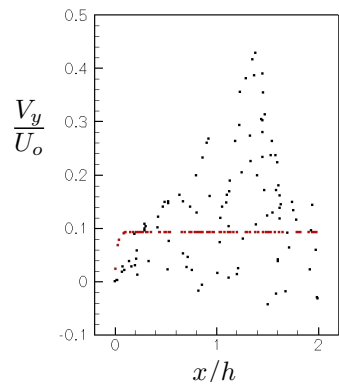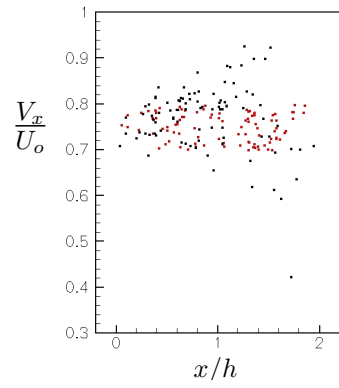
Figure 9: Bubble velocities at a planar cut of $y/h = -0.25$ in laminar channel flow. Euler-Lagrangian results represented by red boxes (□), and the force coupling method results by black boxes (□).

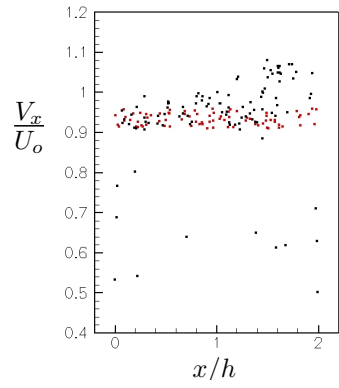Figure 10: Bubble velocities at a planar cut of $y/h = -0.5$ in laminar channel flow. Euler-Lagrangian results represented by red boxes (□), and the force coupling method results by black squares (□).

to travel vertically than the EL bubbles.

The force coupling influence is also observed when comparing the individual bubble velocities. Figures 9-10 plot bubble velocity along x in constant $y-z$ planes. Again, bubbles within a distance of one radii are included. Figure 10 shows the bubble velocities near the wall $(y = -0.5)$. The streamwise velocities fluctuate similarly for both methods. For V_y, the FCM approach shows a wide variation between bubbles, while the EL approach reveals that the bubbles reach a steady-state rise velocity quite rapidly, which remains constant throughout the domain. Also, the FCM bubbles have a some finite but uncorrelated V_z with position, while the EL bubbles have a zero spanwise velocity. Moving upwards in the y-direction, the velocity maximums for the FCM approach become more correlated with increasing streamwise position. For example, for the $y/h = -0.25$ plane, the V_y maximum is at $x = 1.4$, while at $y = -0.5$ plane the maximum velocities are withing the first half of the domain. These peaks in velocity can be attributed to grouping of bubbles rising *en mass*, as discussed above. This feature cannot be reproduced by the one-way coupled Euler-Lagrangian approach.

Conclusion

Two numerical approaches are developed for modeling large systems of bubbles in complex geometries on unstructured grids, with application to modeling sheet-to-cloud cavitation. Both the point-bubble Euler-Lagrangian solver and the extended force coupling method were tested and validated. The Euler-Lagrangian approach is accurate in flows with low bubble concentration, while the force coupling method is able to account for bubble-fluid interactions at large bubble concentrations. As a method to simulate flows with dense and unstable regions of bubble clouds, such as sheet-to-cloud cavitation, the modified force coupling method appears promising. Future work in our efforts towards simulating cavitating flow includes adding a force dipole term and including the general monopole equation for the force coupling method and developing a two-way coupled void-fraction extension to the point-particle Lagrangian method.

Acknowledgments

Nomenclature

Roman symbols

x, y, z	Coordinate axes, coordinates
Re	Reynolds number
We	Weber number
Fr	Froude number
$\vec{g}$	Gravity vector
$\vec{x}$	Eulerian position vector
$R(t)$	Bubble/particle radius
$d(t)$	Bubble/particle diameter
$\vec{Y}(t)$	Bubble/particle position vector
$\vec{u}(\vec{x}, t)$	Fluid velocity vector
$\vec{V}(t)$	Bubble/particle velocity vector
$p(\vec{x}, t)$	Fluid pressure
m	Mass occupied by bubble/particle
C_D	Drag coefficient
U	Reference velocity
S	Surface tension
$\vec{F}(\vec{x}, t)$	Force monopole

Greek symbols

ρ	Density
μ	Dynamic viscosity
ν	Kinematic viscosity
σ_v	Vapor cavitation number
σ	Gaussian length scale
$\vec{\omega}(\vec{x}, t)$	Vorticity vector
Δt	Timestep

Subscripts

$(\ )_f$	of the fluid, used as ρ_f
$(\ )_p$	of the particle, used as ρ_p
$(\ )_b$	of the bubble, used as τ_b
$(\ )_o$	of the freestream, used as U_o
$(\ )_v$	of the vapor, used as p_v

Superscripts

$(\ )^n$	of a specific particle/bubble, used as Y^n

Abbreviations

DNS	Direct Numerical Simulation
EL	Euler-Lagrangian
FCM	Force Coupling Method
LES	Large-Eddy Simulation
SCC	Sheet-to-Cloud Cavitation

References

[1] Babu, P., "Simulation and Modeling of Three Turbulent Flow Problems," Ph.D. Thesis, 2007, Aerospace Engineering & Mechanics, University of Minnesota.

[2] Callenaere, M., Franc, J.P., Michel, J.M., and Riondet, M., "The Cavitation Instability Induced by the Development of a Re-entrant Jet," J. Fluid Mech., Vol. 444, 2001, pp. 223-256.

[3] Dent, G.L., "Aspects of Particle Sedimentation in Dilute Flows at Finite Reynolds Numbers," Ph.D. Thesis, 1999, Brown University, Providence, RI.

[4] Haberman, W.L., and Morton, R.K., "An Experimental Investigation of the Drag and Shape of Air Bubbles Rising in Various Liquids," DTMB Report 802, Sept. 1953.

[5] Johnson, V.E. Jr., and Hsieh, T., " The Influence of the Trajectories of Gas Nuclei on Cavitation Inception," 6th Naval Hydrodynamics Symp., 1966, pp. 163-182.

[6] Lomholt, S., "Numerical Investigations of Macroscopic Particle Dynamics in Microflows," Ph.D. Thesis, 2000, Risø National Laboratory, Roskilde, Denmark.

[7] Lomholt, S., Stenum, B., Maxey, M.R., "Experimental Verification of the Force Coupling Method for Particulate Flows," Int. J. Multiphase Flow., Vol. 28, 2002, pp. 225-246.

[8] Mahesh, K., Constantinescu, G., Moin, P., "A Numerical Method for Large-eddy Simulation in Complex Geometries," J. Comp. Phys., Vol. 197, 2004, pp. 215-240.

[9] Maxey, M.R., Patel, B.K., Chang, E.J., Wang, L.P., "Simulations of Dispersed Turbulent Multiphase Flow," Fluid Dyn. Res., Vol. 20, 1997, pp. 143-156.

[10] Maxey, M.R., Dent, G.L., "Some Features of Particle Sedimentation at Finite Reynolds Numbers," 3rd International Conference on Multiphase Flow, June 1998, Lyon, France.

[11] Maxey, M.R., Patel, B.K., "Localized Force Representations for Particles Sedimenting in Stokes Flow," Int. J. Multiphase Flow, Vol. 27, 2001, pp. 1603-1626.

[12] Maxey, M.R., Riley, J.J., "Equation of Motion for a Small Rigid Sphere in a Nonuniform Flow," Phys. Fluids, Vol. 26, No. 4, 1983, pp. 883-889.